

Measurement of subband electronic temperatures and population inversion in THz quantum-cascade lasers

Miriam S. Vitiello^{a)} and Gaetano Scamarcio^{b)}

INFN Regional Laboratory LIT³ and Dipartimento Interateneo di Fisica "M. Merlin", Università degli Studi di Bari, Via Amendola 173, 70126 Bari, Italy

Vincenzo Spagnolo

INFN Regional Laboratory LIT³ and Dipartimento Interateneo di Fisica "M. Merlin", Politecnico di Bari, Via Amendola 173, 70126 Bari, Italy

Benjamin S. Williams, Sushil Kumar, and Qing Hu

Department of Electrical Engineering and Computer Science and Research Laboratory of Electronics, Massachusetts Institute of Technology, Cambridge, Massachusetts 02139

John L. Reno

Sandia National Laboratories, Department 1123, MS 0601, Albuquerque, New Mexico 87185-0601

(Received 8 November 2004; accepted 1 February 2005; published online 10 March 2005)

We compare the electronic temperatures and the population inversion both below and above the lasing threshold in three quantum-cascade lasers (QCLs) operating at 2.8 THz, 3.2 THz, and 3.8 THz using microprobe band-to-band photoluminescence. In the lasing range, while the ground-state temperature remains close to the lattice one (90 K–100 K), the upper radiative state heats up to ~ 200 K. From the measured thermal resistance and the power dependence of the ground-state electronic temperature, we get a value of the electron-lattice energy relaxation rate comparable with that typical of midinfrared QCLs. © 2005 American Institute of Physics.

[DOI: 10.1063/1.1886266]

Quantum-cascade lasers (QCLs) promise mW-level continuous-wave (cw) power in the range (1–10 THz) for potential applications in spectroscopy, imaging, and sensing. Following the first report, based on chirped superlattices,¹ different schemes have been proposed for the gain medium design, namely, the resonant-phonon,^{2–5} the bound to continuum,⁶ and the interlaced photon-phonon⁷ designs. In this letter, we focus on the resonant-phonon scheme, based on resonant tunneling and fast electron-longitudinal optical (LO) phonon scattering to selectively depopulate the lower radiative state. QCLs based on the above scheme and fabricated with high-confinement low-loss metal waveguides have been demonstrated in the range of 2.1 THz–3.8 THz, and have shown the highest operating temperature in both pulsed (137 K) and cw operation (97 K).^{2–5} While early resonant-phonon QCLs displayed relatively high threshold current densities because of parasitic electronic transport channels,² significant improvements have been obtained using a design aimed at decreasing the parasitic coupling between the injector states and the initial state of the phonon-assisted transition in the next module.³

In this work, we report on the measurement of electronic and lattice temperatures and the relative subband populations in resonant-phonon THz QCLs. Detailed knowledge on the nature of the electronic distribution in THz QCLs is of paramount importance as a guide for the design of improved structures aimed at high-temperature operation. The existence of nonequilibrium electronic distributions in midinfrared (mid-IR) QCLs has been predicted theoretically^{8–10} and assessed experimentally.^{11–13} In THz QCLs, hot-electron dis-

tributions may arise from the detailed balance between the injection and the energy relaxation rates, i.e., inter- and intrasubband electron-electron (e - e), electron-LO phonon, electron-impurity, and interface roughness scattering. At electronic sheet densities $\geq 10^{11}$ cm⁻², the e - e scattering is fast enough to create Boltzmann-type subband distributions characterized by electronic temperatures T_e^i that may exceed the lattice one (T_L) at injected currents close to the laser threshold.^{12,13} Subband thermalization and the related concept of subband temperature is questionable at densities $< 10^9$ cm⁻²,^{8,10} but it still holds at the densities used in THz QCLs (3 – 5×10^{10} cm⁻²).^{9,14}

In THz QCLs, the photon energy is smaller than the LO phonon energy E_{LO} and the electron-LO phonon scattering between radiative subbands is energetically forbidden at very low electronic temperatures (T_e). However, the strong T_e dependence of the nonradiative relaxation rate $\tau_{5 \rightarrow 4}^{-1} \propto \exp[(E - E_{LO})/k_B T_e]$ significantly reduces the gain and increases the threshold current density at high T_e . We show here that optimizing the quantum design may improve the electron-lattice coupling and hence the electrical and optical performance of THz QCLs.⁴

We have compared three QCLs that operate at 2.8 THz (Sample a), 3.2 THz (Sample b), and 3.8 THz (Sample c).^{15,16} The conduction- and valence-band structures for a single period of Sample a are shown in Figs. 1(a) and 1(b); the band structures of Samples b and c are similar. Our experimental method is based on the microprobe band-to-band photoluminescence (PL)¹⁷ that proved successful for the investigation of mid-IR QCLs.^{12,13,18,19} We kept the laser-induced electron heating below a negligible level (~ 3 K) by using an incident optical power of ~ 9 μ W. Thus, the electronic distribution remains unperturbed and the laser excita-

^{a)}Electronic mail: vitiello@fisica.uniba.it

^{b)}Electronic mail: scamarcio@fisica.uniba.it

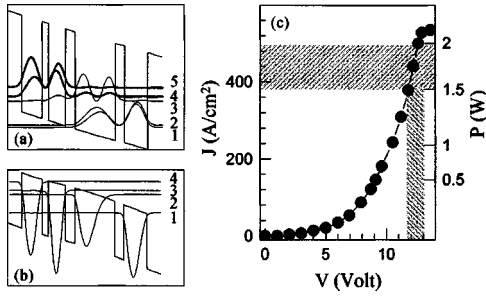


FIG. 1. Conduction (a) and valence (b) band structures of Sample a calculated with a voltage drop of 65 mV per stage using a self-consistent method based on the iterative solution of the Schrödinger and Poisson coupled equations. A 66% conduction-band offset is used. Beginning with the left-most injection barrier, the layer thicknesses measured in Å are 56/81/25/67/39/160/36/93. The underlined layer is doped at $n=1.9 \times 10^{16} \text{ cm}^{-3}$ that corresponds to a sheet density of $3 \times 10^{10} \text{ cm}^{-2}$. The energy levels are labeled using increasing integers starting from the ground state either in the conduction or valence bands. (c) Current density vs voltage characteristic of Sample a measured at the heat sink temperature of 50 K. The shaded area shows the lasing region. The right axis shows the electrical power (P).

tion only provides holes for band-to-band radiative recombination.²⁰ The photoexcited holes quickly relax (~ 200 fs) to one of the valence subbands 1–4 [Fig. 1(b)] and can probe the electron population in the conduction subbands 1–5 [Fig. 1(a)].

Figure 2 shows a set of PL spectra for different values of the electrical power (P). We focus on Sample a, as its P values are sufficiently low to reach the lasing threshold ($P_{\text{th}} \sim 1.5 \text{ W}$, $J_{\text{th}} \sim 400 \text{ A/cm}^2$) well below the maximum heat dissipation rate of our microcryostat. Similar results are found for Samples b and c. Each spectrum shows a main peak that corresponds to the transition $1 \rightarrow 2$ between the injector ground state [level 1 of Fig. 1(a)] and the valence subband 2 [see Fig. 1(b)]. The energy E_p of this peak redshifts with P due to the Joule heating (inset, Fig. 2). To ease the comparison, each spectrum is plotted as a function of the energy difference ΔE with respect to the corresponding E_p value. The structure on the high-energy tail of the peak $1 \rightarrow 2$ is due to the allowed transitions $j \rightarrow k$ between conduc-

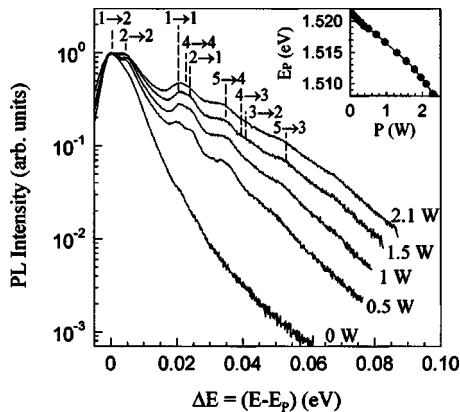


FIG. 2. Representative PL spectra of sample (a) at different electrical powers, each plotted as a function of the energy difference ΔE with respect to the corresponding main peak energy E_p . The heat sink temperature is 50 K. The dashed vertical lines labeled $j \rightarrow k$ mark the energies of the transitions between levels in the conduction (j) and valence (k) bands [see Figs. 1(a) and 1(b)]. Inset: Main peak ($1 \rightarrow 2$) energy E_p as a function of the electrical power. The line is a guide for the eyes.

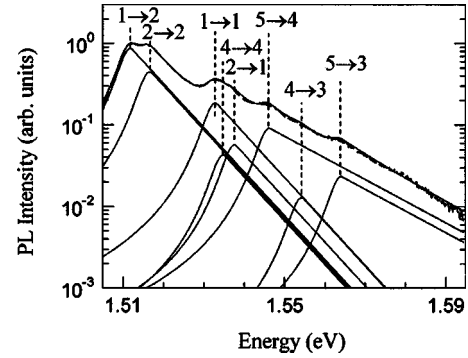


FIG. 3. Dashed line: PL spectrum at $P=1.5 \text{ W}$. Solid line: Calculated PL components peaked at the theoretical energies of relevant $j \rightarrow k$ transition [see Figs. 1(a) and 1(b)]. The low-energy side of each curve is a Lorentzian with half width at half maximum = 3.2 meV. The high-energy side is an exponential decay function $\propto \exp[-(E - E_{j \rightarrow k})/k_B T_e^j]$.

tion and valence subbands by comparison with the calculated energies E_{jk} .

The analysis of the PL line shape is based on the following expression:

$$I_{\text{PL}}(E) \propto \sum_{j=1}^5 \sum_{k=1}^4 A_{jk} E_{jk}^4 \langle \psi_j | \psi_k \rangle^2 \mathcal{L}(E), \quad (1)$$

where $A_{jk} = n_j \cdot p_k$, n_j , and p_k are the populations of the conduction and valence subbands. The term $\langle \psi_j | \psi_k \rangle$ is the overlap integral of the envelope functions. The line shape function $\mathcal{L}(E)$ is obtained joining a Lorentzian with a phenomenological broadening $\Gamma/2 = 3.2 \text{ meV}$ on the low-energy side, and an exponential decay $\propto \exp[-E/k_B T_e^j]$ on the high-energy side. T_e^j is the electronic temperature of the conduction j th subband. For $P \geq 1 \text{ W}$, an excellent reproduction of the PL is obtained considering the $j \rightarrow k$ transitions that have an overlap integral > 0.2 and leaving $T_e^j A_{jk}$ as fitting parameters. Figure 3 illustrates the application of this method for the PL spectrum of Sample a measured at $P=1.5 \text{ W}$.²¹ However, for $P < 1 \text{ W}$, the results becomes unclear, since the number of allowed transitions considerably increases due to the lower localization of the wave function $j=5$ and the occurrence of resonances between subbands originating in adjacent periods. Therefore, in the range $P < 1 \text{ W}$ we have restricted our analysis to the main PL band and estimated only the ground-state electronic temperature.

The fitting parameters T_e^j are plotted in Fig. 4(a) as a function of P together with T_L , extracted by comparing E_p against a calibration curve obtained by probing the device with zero injected-current while varying the heat sink temperature.¹⁹ We found that the electronic temperatures of the subbands $j=1-4$ are nearly equal and increase linearly with P with a slope $R_e = 28.0 \text{ K/W}$, slightly larger than the thermal resistance $R = dT_L/dP = 25.3 \text{ K/W}$.²² On the other hand, the temperature of the upper laser level T_e^5 reaches $\sim 200 \text{ K}$ in the range of $P=1 \text{ W}-2.2 \text{ W}$, i.e., it is higher by $\sim 100 \text{ K}$ than T_L . The existence of differences as high as 25–40% in the subband electronic temperatures is predicted by Monte Carlo simulations both in mid-IR¹⁰ and THz²³ QCLs. In our case, we tentatively ascribe the large difference between T_e^5 and $T_e^{1,2}$ to the reduced efficiency of intersubband $e-e$ scattering channels coupling electrons in the $j=5$ and $j=1,2$ levels, with respect to intrasubband $e-e$ processes, as calculated for prototype THz QCLs structures.¹⁴ One impor-

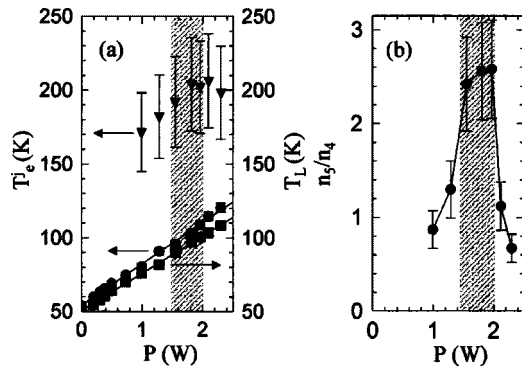


FIG. 4. (a): Mean lattice temperature (■) and electronic temperatures T_e^j ; $j=1,2$ (●); $j=5$ (▼) in the active region of Sample a measured as a function of the electrical power at a heat sink temperature of 50 K. The lines are linear fits to the data. The small difference (~ 3 K) between T_e and T_L at zero-electrical power is a well known effect due to the heating of the electronic ensemble induced by the probe laser. (b) Relative populations n_5/n_4 between the upper ($j=5$) and lower ($j=4$) laser level as a function of the dissipated electrical power calculated for Sample a. The shaded areas mark the lasing region.

tant implication of our findings is that the high T_e^5 values lead to relatively fast nonradiative relaxation times $\tau_{5 \rightarrow 4,3} \approx 1.3$ ps, and thus it is a key limiting factor for the operation at high temperatures of the investigated THz QCLs.

The expression $(R_e - R)^{-1}$ gives the strength of the electron-lattice energy relaxation rate $(\tau_E)^{-1}$. In resonant-phonon THz QCLs, the latter rate is controlled by the LO-phonon-assisted transitions $3,4 \rightarrow 1,2$. Simple rate equation arguments give $\tau_E^{-1} = P/N_e N k_B (T_e - T_L)$, where N_e is the number of electrons per stage and N is the number of stages. Since we have shown in our system that the vast majority of electrons share the same temperature, we can rewrite $\tau_E^{-1} = [N_e N k_B (R_e - R)]^{-1}$. From the measured R_e and R values, we obtained $\tau_E^{-1} = 4.9$ ps $^{-1}$, $\tau_E^{-1} = 1.67$ ps $^{-1}$, and $\tau_E^{-1} = 1.05$ ps $^{-1}$ for Samples a, b, and c, respectively. The largest electron-lattice coupling for Sample a confirms the efficacy of its design that has been aimed at increasing the matrix elements associated with the $3,4 \rightarrow 1,2$ transitions. Also, the energy separation between the above levels is slightly higher than E_{LO} at all values of the electric field above the alignment. The more efficient carrier thermalization in Sample a reduces thermal backfilling of the subband $j=4$, helps in keeping the optical gain closer to the designed value, and thus improves optical performance. In fact, the larger τ_E values in Samples b and c, respectively, are reflected in the higher measured laser thresholds: $J_{th} = 450$ A/cm 2 and $J_{th} = 630$ A/cm 2 .

Figure 4(b) shows the ratio n_5/n_4 as a function of P for Sample a, determined from the ratio A_{54}/A_{44} . The population inversion ($n_5/n_4 > 1$) occurs when P is slightly > 1 W, in agreement with the measured laser threshold of ~ 1.5 W. It then starts to decrease beyond 2.0 W where the injector subbands become misaligned with the $j=5$ level, the device enters a region of negative differential resistance, and lasing ceases. The fact that n_5/n_4 remains approximately constant during laser operation likely reflects the clamping of the gain (and thus the population inversion $n_5 - n_4$) that occurs at lasing threshold.

In conclusion, we note that optimizing the phonon-mediated transitions ($3 \rightarrow 2$, $3 \rightarrow 1$) in THz QCLs leads to electron-lattice energy relaxation rates comparable with

those of mid-IR QCLs ($\tau_E^{-1} = 4$ ps $^{-1}$).¹³ However, the performance is limited by the hot electron distribution in the upper radiative state.

This work was partly supported by MIUR (FIRB-RBAU01E8SS), ESA-ESTEC(16863/02/NL/PA), and by AFOSR, NASA, and NSF at MIT. One of the authors (B.W.) would like to thank H. Callebaut for helpful discussions. Sandia is a multiprogram laboratory operated by Sandia Corporation, a Lockheed-Martin Company, for the U. S. Dept. of Energy (Contract No. DE-AC04-94AL85000).

- ¹R. Köhler, A. Tredicucci, F. Beltram, H. E. Beere, E. H. Linfield, A. G. Davies, D. A. Ritche, R. C. Iotti, and F. Rossi, *Nature (London)* **417**, 156 (2002).
- ²B. S. Williams, S. Kumar, H. Callebaut, Q. Hu, and J. L. Reno, *Appl. Phys. Lett.* **83**, 5142 (2003).
- ³S. Kumar, B. S. Williams, S. Kohen, Q. Hu, and J. L. Reno, *Appl. Phys. Lett.* **84**, 2494 (2004).
- ⁴Q. Hu, B. S. Williams, S. Kumar, H. Callebaut, S. Kohen, and J. L. Reno (unpublished).
- ⁵B. S. Williams, S. Kumar, Q. Hu, and J. L. Reno, *Electron. Lett.* **40**, 431 (2004).
- ⁶L. Ajili, G. Scarlari, J. Faist, H. E. Beere, E. H. Linfield, A. Ritchie, and A. G. Davies, *Appl. Phys. Lett.* **85**, 3986 (2004).
- ⁷R. Köhler, A. Tredicucci, F. Beltram, H. E. Beere, E. H. Linfield, A. Ritchie, and A. G. Davies, *Appl. Phys. Lett.* **84**, 1266 (2004).
- ⁸V. B. Gorfinkel, S. Luryi, and B. Gelmont, *IEEE J. Quantum Electron.* **32**, 1995 (1996).
- ⁹P. Harrison, *Appl. Phys. Lett.* **75**, 2800 (1999).
- ¹⁰R. C. Iotti and F. Rossi, *Appl. Phys. Lett.* **78**, 2902 (2001).
- ¹¹M. Troccoli, G. Scamarcio, V. Spagnolo, A. Tredicucci, C. Gmachl, F. Capasso, D. L. Sivco, and M. Striccoli, *Appl. Phys. Lett.* **77**, 1088 (2000).
- ¹²V. Spagnolo, G. Scamarcio, W. Schrenk, and G. Strasser, *Semicond. Sci. Technol.* **19**, 1 (2004).
- ¹³V. Spagnolo, G. Scamarcio, H. Page, and C. Sirtori, *Appl. Phys. Lett.* **84**, 3690 (2004).
- ¹⁴P. Harrison and R. W. Kelsall, *Solid-State Electron.* **42**, 1449 (1998).
- ¹⁵All devices are composed of a 10 μm thick GaAs/Al $_{0.15}$ Ga $_{0.85}$ active region grown by molecular-beam epitaxy on a semi-insulating GaAs substrate. The samples were processed into metal-metal waveguide structures using either Cu-Cu (Sample a), or In-Au (Samples b and c) wafer bonding techniques. Ridge waveguides were defined using photolithography and reactive ion etching. Sample a was 40 μm wide and 0.72 mm long, Sample b was 80 μm wide and 0.82 mm long, and Sample c was 100 μm wide and 1.09 mm long.
- ¹⁶B. S. Williams, S. Kumar, H. Callebaut, Q. Hu, and J. L. Reno, *Appl. Phys. Lett.* **83**, 2124 (2003).
- ¹⁷The devices were mounted on the cold finger of a helium-flow microcryostat using thermal grease to improve the thermal contact. The heat sink temperature was controlled by a Si-diode mounted close to the laser die. The 647 nm line of a Kr $^+$ laser was focused to a 2.5 μm spot onto the laser front facet.
- ¹⁸V. Spagnolo, M. Troccoli, G. Scamarcio, C. Gmachl, F. Capasso, A. Tredicucci, A. M. Sergent, A. L. Hutchinson, D. L. Sivco, and A. Y. Cho, *Appl. Phys. Lett.* **78**, 2095 (2001).
- ¹⁹V. Spagnolo, G. Scamarcio, D. Marano, M. Troccoli, F. Capasso, C. Gmachl, A. M. Sergent, A. L. Hutchinson, D. L. Sivco, A. Y. Cho, H. Page, C. Becker, and C. Sirtori, *IEEE Proc. J. Optoelectron.* **150**, 298 (2003).
- ²⁰The estimated density of photogenerated carriers is $\Delta n = 0.7 - 1.1 \times 10^{15}$ cm $^{-3}$. These limits have been calculated using the values 1-2 ns and 5-7 μm for the carrier lifetime and the diffusion length, respectively.
- ²¹Note that the transition $3 \rightarrow 2$ does not contribute to the luminescence, despite the large value of the overlap integral ($\langle \psi_3 | \psi_2 \rangle = 0.4 - 0.5$) in the whole range of investigated powers and thus demonstrates that the electron-LO phonon interaction efficiently depletes the subband $j=3$.
- ²²The thermal resistance of Devices b and c are $R = 18.6$ K/W and $R = 18.0$ K/W. These values are 2.5-3.5 times larger than in mid-IR QCLs, due to the thicker active layers used for THz QCLs.
- ²³H. Callebaut, S. Kumar, B. S. Williams, Q. Hu, and J. L. Reno, *Appl. Phys. Lett.* **83**, 207 (2003).